Numerical simulations of the Princeton magnetorotational instability experiment with conducting axial boundaries

Xing Wei,[1] Hantao Ji,[1,2] Jeremy Goodman,[1] Fatima Ebrahimi,[2] Erik Gilson,[2] Frank Jenko,[3] and Karl Lackner[4]

[1]*Princeton University Observatory, Princeton, New Jersey 08544, USA*
[2]*Princeton Plasma Physics Laboratory, Princeton, New Jersey 08540, USA*
[3]*UCLA Physics and Astronomy, Los Angeles, California 90095, USA*
[4]*Max Planck Institute for Plasma Physics, D-85748 Garching bei München, Germany*

We investigate numerically the Princeton magnetorotational instability (MRI) experiment and the effect of conducting axial boundaries or endcaps. MRI is identified and found to reach a much higher saturation than for insulating endcaps. This is probably due to stronger driving of the base flow by the magnetically rather than viscously coupled boundaries. Although the computations are necessarily limited to lower Reynolds numbers (Re) than their experimental counterparts, it appears that the saturation level becomes independent of Re when Re is sufficiently large, whereas it has been found previously to decrease roughly as $Re^{-1/4}$ with insulating endcaps. The much higher saturation levels will allow for the positive detection of MRI beyond its theoretical and numerical predictions.

I. INTRODUCTION

Magnetorotational instability (MRI) was discovered by Velikhov [1], more systematically studied by Chandrasekhar [2], and applied to accretion disks by Balbus and Hawley [3]. Since the specific angular momentum (Ωr^2) of such disks increases outward, they are hydrodynamically stable against Rayleigh's axisymmetric centrifugal instability. Numerical [4,5] and experimental [6,7] evidence indicates that generic Keplerian and quasi-Keplerian flows are completely stable against purely hydrodynamic modes. It is therefore believed that the turbulence and angular-momentum transport in accretion disks is driven mainly by MRI [8]. The Princeton MRI experiment has been designed to demonstrate the instability in a Taylor-Couette flow [9–11]. Relevant linear-stability analyses have been carried out at various levels of geometric fidelity [12–14]. Nonlinear calculations have been performed in axisymmetry with periodic boundary conditions [15] or insulating boundary conditions [16] and in three dimensions with pseudovacuum boundary conditions [17]. The latter found that the saturation level of MRI decreases roughly as $Re^{-1/4}$ with increasing Reynolds number (Re) at fixed magnetic Reynolds number (Rm). This can be explained heuristically by balancing viscous interaction at the boundaries against magnetic stresses in the bulk fluid. It was then considered that conducting endcaps may improve MRI. A linear boundary-layer calculation in the spirit of [18] but for a conducting boundary (see also [19,20]) gives the ratio of magnetic to viscous boundary-layer stresses as

$$\frac{\Gamma_{\text{mag}}}{\Gamma_{\text{visc}}} = \frac{\sqrt{2}\Lambda}{(1+\Lambda^2)^{1/4}} \left(\frac{\Omega\delta^2}{\nu}\right)^{1/2}. \qquad (1)$$

Here $\Lambda = \sigma_f B_0^2/\rho\Omega$ is an Elsasser number based on the fluid conductivity (σ_f) and density (ρ), the imposed field normal to the boundary (B_0), and the angular velocity Ω, which is assumed to be slightly different for the boundary than for the fluid at large distances from it. The conductivity (σ_s) and geometrical thickness (d_s) of the boundary enter this expression via an effective electrical thickness $\delta = \sigma_s d_s/\sigma_f$. In the experimental parameter regime, the ratio (1) is $\sim 10^3$, i.e., the magnetic coupling is 1000 times stronger than viscous coupling.

In this work, we use numerical calculations to test the effect of conducting endcaps on the MRI saturation level and other aspects of the flow. The basic equations are discussed in Sec. II, results in Sec. III, and experimental implications in Sec. IV.

II. EQUATIONS

We solve the dimensionless Navier-Stokes and induction equations

$$\frac{\partial \boldsymbol{u}}{\partial t} + \boldsymbol{u} \cdot \nabla \boldsymbol{u} = -\nabla p + \frac{1}{\text{Re}}\nabla^2 \boldsymbol{u} + (\nabla \times \boldsymbol{B}) \times \boldsymbol{B}, \qquad (2)$$

$$\frac{\partial \boldsymbol{B}}{\partial t} = \nabla \times (\boldsymbol{u} \times \boldsymbol{B}) + \frac{1}{\sigma \text{Rm}}\nabla^2 \boldsymbol{B}, \qquad (3)$$

using cylindrical coordinates (r,θ,z) in a domain modeled after the Princeton MRI experimental setup, where the inner and outer cylinders have radii $r_1 = 7$ cm and $r_2 = 21$ cm, the height $h = 28$ cm, and the thickness of the newly installed copper endcaps $d_s = 2$ cm [11]. The magnetic induction equation is solved for both fluid and solid endcaps. A quasispherical vacuum region in which $\boldsymbol{B} = \nabla\Psi$ surrounds the walls and endcaps, and on the outer boundary of this region we set the magnetic potential $\Psi = B_0 z$. The radius of the spherical vacuum is ten times the height of the cylindrical setup.

The computational units of length, time, magnetic field, and conductivity are r_1, Ω_1^{-1}, $r_1\Omega_1\sqrt{\rho\mu_0}$, and σ_f of the working liquid metal GaInSn, respectively. Here Ω_1 is the angular velocity of the inner cylinder and ρ is the density of the fluid. Note that all permeabilities have the vacuum value, μ_0. The three dimensionless parameters governing this magnetohydrodynamic system are the Reynolds number $\text{Re} \equiv \Omega_1 r_1^2/\nu$, the magnetic Reynolds number $\text{Rm} \equiv \Omega_1 r_1^2 \sigma_f \mu_0$, and the Lehnert number $B_0 \equiv V_A/\Omega_1 r_1 = \tilde{B}_0/\sqrt{\rho\mu_0}\Omega_1 r_1$, where $\tilde{B}_0$ is the imposed field in dimensional units. Other dimensionless measures of the field strength can be expressed in terms of the Lundquist number $\text{Lu} \equiv V_A r_1 \mu_0 \sigma_f = B_0 \text{Rm}$,

the Elsasser number $\Lambda \equiv V_A^2/\eta\Omega = B_0^2 \mathrm{Rm}$, and the Hartmann number $\mathrm{Ha} \equiv r_1 V_A \sqrt{\mu_0 \sigma_f/\nu} = B_0\sqrt{\mathrm{Re\,Rm}}$. The experimental design limit for Ω_1 is 4000 rpm, and so $\mathrm{Re} \sim O(10^7)$, $\mathrm{Rm} \sim O(10)$, and $B_0 \sim O(0.1)$. The dimensionless thickness of the endcaps is $d_s = 0.3$ (approximately), and their electrical conductivity is $\sigma_s = 19$.

In the regime where MRI occurs but centrifugal instability does not, it is required that $\Omega_1 > \Omega_2$ but $r_1^2\Omega_1 < r_2^2\Omega_2$:

the "quasi-Keplerian" regime. Inserting $r_2 = 3r_1$ we are led to the condition for MRI, $1/9 < \Omega_2/\Omega_1 < 1$. In the calculations we take $\Omega_2/\Omega_1 = 0.1325$. To suppress Ekman (or Ekman-Hartmann) circulation driven by the boundary layers at the endcaps, both in these calculations and in the actual experiment, the endcaps are divided into two rings. No-slip conditions are applied at the boundaries, with angular velocities

$$\Omega_1 = 1, \quad r = 1, \ -2 \leqslant z \leqslant 2: \text{ inner cylinder;}$$
$$\Omega_3 = 0.55, \quad 1 < r < 2, \ z = -2,2: \text{ inner ring;}$$
$$\Omega_2 = 0.1325, \quad r > 2: \text{ outer ring } (z = 0,h) \text{ and cylinder } (r_2 = 3). \tag{4}$$

The initial fluid velocity is piecewise uniform rotation matched to the rings. The initial magnetic field is the imposed uniform vertical field B_0. Following [17], departures from this initial field configuration are quantified by the volume-averaged radial field ("B_r signal"):

$$\sqrt{\frac{1}{V}\int_V \left(\frac{B_r}{B_0}\right)^2 dV}. \tag{5}$$

The numerical calculations are carried out with the spectral finite element Maxwell Navier-Stokes solver (SFEMANS) [21]. A Fourier spectral method is used in azimuth (θ), and finite elements in the meridional plane. In the experimentally accessible regime, MRI is expected to be axisymmetric, and so the calculations presented here are axisymmetric, although some nonaxisymmetric calculations were made to test for shear layer instabilities [17,22,23]. Up to 18 000 triangular finite elements were used in the meridional plane.

III. RESULTS

The endcaps drive secondary circulation, so that MRI must be detected as a modification or bifurcation of the circulation rather than a linear instability [17]. Calculations at the experimental $\mathrm{Re} \sim 10^7$ would be prohibitive, so we begin by seeking MRI at $\mathrm{Re} = 1000$ and later study trends up to $\mathrm{Re} = 32\,000$.

Figure 1(a) shows the B_r signal versus B_0 for different Rm. The B_r signal reaches its maximum at the intermediate B_0 but is weak at both low and high B_0. This result is consistent with the fact that MRI needs magnetic field but will be suppressed by a strong field [2], and it is also consistent with the onset of MRI predicted by the local analysis [12], the global analysis [13], and the numerical calculation with pseudovacuum boundary condition [17]. Figure 1(b) shows the linear growth rate versus B_0 predicted by the methods of [13] for the same Re in vertically periodic cylinders with vertical wavelength $2h$, which approximates the magnetic geometry at saturation (Fig. 2). Evidently, the B_r signal at saturation and the expected MRI linear growth rate have similar dependence on the field strength.

To suppress meridional circulation and isolate MRI signatures, we have also performed simulations in which the rotation of the insulating endcaps follows the ideal

Taylor-Couette flow profile, $\Omega(r) = a + b/r^2$. Although not feasible experimentally, such differentially rotating endcaps would permit a basic state of purely azimuthal motion following the ideal profile at all heights, and deviations could be interpreted as evidence for MRI (or perhaps other instabilities) rather than Ekman circulation. Figure 1(c) shows the B_r signal versus B_0 for these simulations. Note that the B_r signal vanishes as $B_0 \to 0$, unlike Fig. 1(a), as one expects in the absence of Ekman circulation. Apart from this, the general similarity of panels (a) and (c) suggests that the B_r signal in both cases is dominated by MRI, or at least not by meridional circulation of the basic state. We also tested conducting endcaps with the smoothly varying rotational profile of ideal Taylor-Couette flow, and the results are slightly different from the previous insulating endcaps (the difference arises from the numerical error of the code). This suggests that the higher saturation levels of MRI with conducting endcaps may be due to the stronger driving of the base flow by conducting endcaps.

Figure 1(d) shows the dependence of B_r on Rm at several B_0. For the three weaker fields, the variation with Rm is monotonic but changes slope at an Rm that itself decreases with B_0: at $\mathrm{Rm} \approx 9$ for $B_0 = 0.10$, at $\mathrm{Rm} \approx 8$ for $B_0 = 0.15$, and at $\mathrm{Rm} \approx 4$ for $B_0 = 0.25$. It is known that B_r can be induced by either the Ekman-Hartmann circulation or MRI, and moreover, in different parameter regimes the circulation-induced B_r and the MRI-induced B_r may depend differently on the dimensionless parameters. At least in uniform rotation, the thickness of the boundary layer and the mass flux through it decrease monotonically with increasing Elsasser number ($B_0^2 \mathrm{Rm}$) at fixed Re [18,20], and the B_r signal behaves similarly. MRI, on the other hand, grows fastest at intermediate B_0, as Fig. 1(b) illustrates. Therefore, we take the data in Fig. 1 as evidence for the onset of MRI.

Figure 2 shows the meridional distributions of u_r, u_z, B_r, and B_z at $\mathrm{Re} = 1000$, $\mathrm{Rm} = 20$, and $B_0 = 0.15$, which is well within the MRI regime as discussed above, i.e., $\mathrm{Rm} > \mathrm{Rm}_c = 8$ for $B_0 = 0.15$ as shown by Fig. 1(d). Figure 2(a) shows that the radial flow mainly lies in the boundary layer. Figure 2(b) shows the pumping arising from the Ekman-Hartmann boundary layer. The combination of Figs. 2(a) and 2(b) shows the pattern of circulation, i.e., in two opposing cells, clockwise at $z > 0$ and counterclockwise at $z < 0$. Figure 2(c) shows that B_r varies almost monotonically with
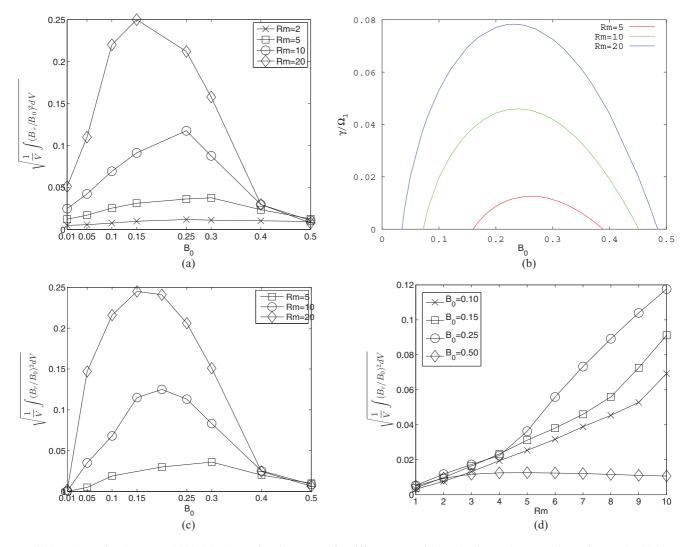
FIG. 1. The B_r signal at Re $= 1000$. (a) The B_r signal versus B_0 for different Rm, with conducting endcaps rotating as in Eq. (4). (b) Linear growth rate of MRI versus B_0 for periodic vertical boundary conditions with period $2h$. (c) Like (a) but for insulating endcaps rotating with the ideal Taylor-Couette profile. (d) The B_r signal versus Rm for different B_0, with endcaps as in (a).
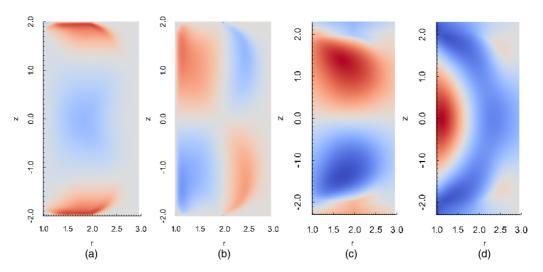

FIG. 2. Meridional distributions. (a) The radial velocity u_r. (b) The axial velocity u_z. (c) The radial field B_r. (d) The axial field B_z. Conducting endcaps at Re $= 1000$, Rm $= 20$, and $B_0 = 0.15$.
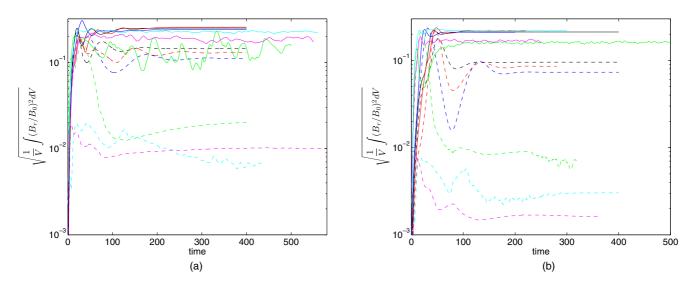
FIG. 3. Conducting and insulating endcaps at Rm = 20. (a) The B_r signal versus time for different Re at $B_0 = 0.15$. (b) The B_r signal versus time for different Re at $B_0 = 0.25$. Solid lines denote conducting endcaps and dashed lines denote insulating endcaps. Black, red, blue, green, magenta, and cyan colors correspond, respectively, to Re = 1000, 2000, 4000, 8000, 16 000, and 32 000. Time unit is Ω_1^{-1}.

height and the strongest B_r appears at $z \approx \pm 1.5$ away from the boundary layer where the strongest u_r appears. The different locations of the strongest B_r and u_r suggest that B_r is mainly induced not by circulation (i.e., interaction of u_r and B_0) but by MRI. Figure 2(d) shows that the strongest B_z appears at the midplane $z = 0$, where u_z is almost zero. Again, this suggests that B_z is mainly induced not by circulation (i.e., interaction of u_z and B_r) but by MRI.

We have also made calculations at higher Re, in order to extrapolate toward the experimental regime. Figure 3 shows the time evolution of the B_r signal at Rm = 20 for different Re and magnetic boundary conditions. The left and right panels are for, respectively, $B_0 = 0.15$ and 0.25, and both of them are in the MRI regime. With insulating endcaps, the B_r signal becomes almost time independent after the initial

transient. With conducting endcaps, the B_r signal fluctuates for Re $\geqslant 8000$. The variation of the time-averaged B_r signal with Re is shown in Fig. 4. Clearly, the B_r signal is higher with conducting than with insulating endcaps, and the contrast increases with increasing Re (Fig. 4). At the highest Re = 3.2×10^4, the B_r signal with conducting endcaps is around 30 (70) times that with insulating endcaps for $B_0 = 0.15$ (0.25). This is qualitatively consistent with Eq. (1). The B_r signal scales differently with Re for the two boundary conditions. With insulating endcaps the B_r signal decreases with increasing Re, though more slowly above Re = 8000. With the conducting endcaps, the signal is approximately constant at large Re, as might be expected if the flow is sustained mainly by magnetic rather than viscous coupling to the boundaries.
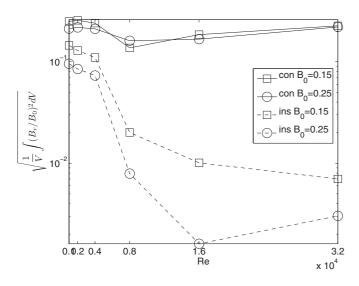

FIG. 4. The B_r signal at Rm = 20 versus Re for different B_0 and magnetic boundary conditions, as in Fig. 3.
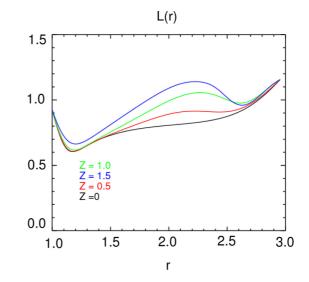

FIG. 5. The radial profile of specific angular momentum $L \equiv r^2\Omega$ at several heights, as marked. Other parameters (Re, Rm, B_0) as in Fig. 2.
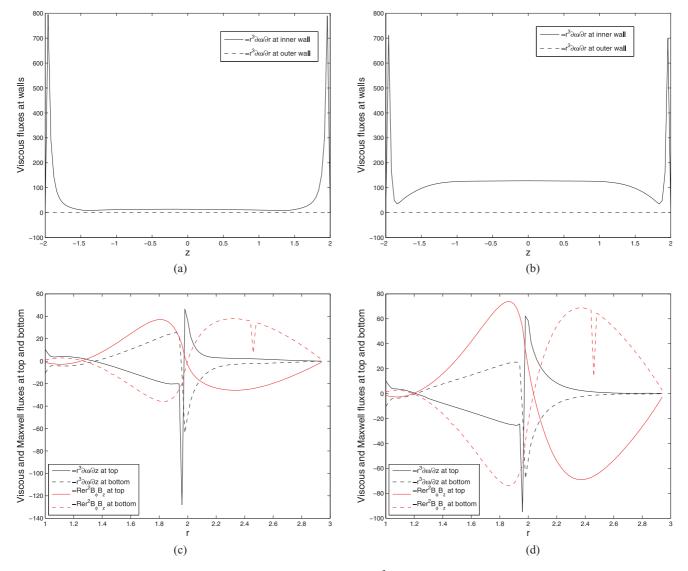
FIG. 6. Viscous and Maxwell fluxes. (a) and (b): radial viscous fluxes $-r^3 \partial\omega/\partial r$ at the inner and outer walls. (c) and (d): axial viscous fluxes $-r^3 \partial\omega/\partial z$ and Maxwell fluxes $-\mathrm{Re}r^2 B_\phi B_z$ at the top and bottom. Rm = 10 for (a) and (c) and Rm = 20 for (b) and (d). Re = 1000 and $B_0 = 0.15$.

IV. DISCUSSION

In this work we carried out the preliminary numerical calculations for the Princeton MRI experiment to test the effect of conducting (copper) endcaps. Although the fluid Reynolds number of the numerical calculations is far away from the experimental regime, Re $= O(10^7)$, these calculations have guided the redesign of the experiment. Firstly, MRI has been identified in a regime of intermediate B_0 and modest Rm. According to these calculations, with conducting endcaps, MRI is very likely to be discovered at Rm $\geqslant 5$ and $B_0 \approx$ 0.2–0.3. In the experiment, the maximum Rm reaches 9 and B_0 can be selected within the range 0–0.3. Secondly, conducting endcaps greatly increase the MRI signal, to a level $\sim 20\%$ at experimentally accessible Rm and B_0. This is sufficiently strong to be detected by the Hall probe newly installed on the experimental setup.

The discontinuous rotation profile (4), if it extends from the endcaps into the fluid (forming a so-called Shercliff layer),

might be expected to excite nonaxisymmetric instabilities of the Kelvin-Helmholtz type [11,22]. To test this, nonaxisymmetric simulations were performed with azimuthal wave numbers up to $m = 4$ and Reynolds numbers up to Re = 32 000. Negligible energy was found in the nonaxisymmetric components ($m > 0$). This is in accord with the experimental results of [11], who found that Shercliff-layer instabilities grow robustly in this apparatus (but before the endcaps were made conducting) only when the Elsasser number $\Lambda = \sigma \tilde{B}_0^2/\rho\Omega$ is $\geqslant 1$, whereas $\Lambda \lesssim 1$ in the simulations of this paper.

Also possibly relevant is Rayleigh's centrifugal instability, which may arise where the specific angular momentum decreases outward, $\partial |r^2\Omega|/\partial r < 0$. We plot the radial angular-momentum profile in Fig. 5 for the same parameters as in Fig. 2. Evidently, the angular momentum increases radially outward except near the inner cylinder, $1.0 < r <$ 1.2, and at $2.3 \lesssim r \lesssim 2.6$. According to Fig. 2(c), however, B_r is largest at $1.5 \lesssim r \lesssim 2.0$, where the flow is locally

centrifugally stable ($d|L|/dr > 0$). In short, it seems unlikely that the B_r signal is dominated by Shercliff-layer or Rayleigh instabilities.

To summarize, we have the following evidence for the presence of MRI in our simulations:

(1) the similarity of the normalized B_r signal at nonlinear saturation to the linear MRI growth rate—in particular, the monotonic dependence on magnetic Reynolds number Rm and nonmonotonic dependence on the background field B_0 [Fig. 1(b)];

(2) the similarity of the signal to that obtained in simulations where Ekman simulation is suppressed [Fig. 1(c)];

(3) a change in the slope of the dependence of the signal on Rm at the predicted threshold of MRI [Fig. 1(d)];

(4) different spatial distributions of radial velocity u_r (largest near boundaries) and radial field B_r (largest in the bulk) (Fig. 2);

(5) absence of nonaxisymmetric modes; and

(6) lack of spatial correlation of the signal with conditions favoring centrifugal instability.

To end this paper we briefly discuss the flux of axial angular momentum. In the axisymmetric case, the radial and axial components of this flux are

$$F_r = \rho r \left(u_r u_\phi - \frac{B_r B_\phi}{\rho \mu_0} - \nu r \frac{\partial \omega}{\partial r} \right),$$

$$F_z = \rho r \left(u_\phi u_z - \frac{B_\phi B_z}{\rho \mu_0} - \nu r \frac{\partial \omega}{\partial z} \right), \quad (6)$$

where $\omega = u_\phi / r$ is the angular velocity. In a steady state, or in the time average, $\nabla \cdot \boldsymbol{F} = 0$, and the flux integrated over the boundaries should vanish. Since the Reynolds stresses $u_r u_\phi$ and $u_\phi u_z$ vanish at the boundaries, we compare the viscous and Maxwell fluxes. We normalize the stresses with $\nu \Omega_1$ such that a prefactor Re appears in the dimensionless expression of the Maxwell fluxes. We are concerned with the viscous

and Maxwell fluxes across the boundaries, namely, $2\pi r F_r$ versus z at $r = r_1$ and r_2 and $2\pi r F_z$ versus r at $z = \pm h/2$. Figure 6 shows the radial fluxes at the inner and outer walls [Figs. 6(a) and 6(b)], and the axial fluxes at the top and bottom endcaps [Figs. 6(c) and 6(d)] at Rm = 10 and 20. For the radial fluxes, the Maxwell fluxes vanish because the walls are insulating and the viscous flux at the inner wall dominates over the one at the outer wall. At the endcaps, the magnetic flux is lower than the viscous at the low Rm = 10 but exceeds the viscous at the large Rm = 20. Figures 6(c) and 6(d) show that both the viscous and Maxwell fluxes change their signs between the inner and outer rings. The integral of the difference between the top and bottom endcaps is greater than that between the outer and inner walls, and thus the transport of angular momentum is substantially axial rather than purely radial. This is not what is usually envisaged for MRI transport in accretion disks. However, in the disks of protostars (and perhaps other disks, including those of quasars), much of the angular momentum may be removed via magnetic stresses that couple to an outflow (magnetocentrifugal wind), and in some parameter regimes this may be accompanied by MRI turbulence within the disk [24].

[1] E. P. Velikhov, Stability of an ideally conducting liquid flowing between rotating cylinders in a magnetic field, Sov. Phys. JETP **36**, 1398 (1959).

[2] S. Chandrasekhar, *Hydrodynamic and Hydromagnetic Stability* (Oxford University Press, New York, 1961).

[3] S. A. Balbus and J. F. Hawley, A powerful local shear instability in weakly magnetized disks. I - Linear analysis. II - Nonlinear evolution, Astrophys. J. **376**, 214 (1991).

[4] J. F. Hawley, S. A. Balbus, and W. F. Winters, Local hydrodynamic stability of accretion disks, Astrophys. J. **518**, 394 (1999).

[5] G. Lesur and P.-Y. Longaretti, On the relevance of subcritical hydrodynamic turbulence to accretion disk transport, Astron. Astrophys. **444**, 25 (2005).

[6] H. Ji, M. Burin, E. Schartman, and J. Goodman, Hydrodynamic turbulence cannot transport angular momentum effectively in astrophysical disks, Nature (London) **444**, 343 (2006).

[7] E. M. Edlund and H. Ji, Nonlinear stability of laboratory quasi-Keplerian flows, Phys. Rev. E **89**, 021004(R) (2014).

[8] S. A. Balbus and J. F. Hawley, Instability, turbulence, and enhanced transport in accretion disks, Rev. Mod. Phys. **70**, 1 (1998).

[9] A. Kageyama, H. Ji, J. Goodman, F. Chen, and E. Shoshan, Numerical and experimental investigation of circulation in short cylinders, J. Phys. Soc. Jpn. **73**, 2424 (2004).

[10] M. D. Nornberg, H. Ji, E. Schartman, A. Roach, and J. Goodman, Observation of Magnetocoriolis Waves in a Liquid Metal Taylor-Couette Experiment, Phys. Rev. Lett. **104**, 074501 (2010).

[11] A. H. Roach, E. J. Spence, C. Gissinger, E. M. Edlund, P. Sloboda, J. Goodman, and H. Ji, Observation of a Free-Shercliff-Layer Instability in Cylindrical Geometry, Phys. Rev. Lett. **108**, 154502 (2012).

[12] H. Ji, J. Goodman, and A. Kageyama, Magnetorotational instability in a rotating liquid metal annulus, Mon. Not. R. Astron. Soc. **325**, L1 (2001).

[13] J. Goodman and H. Ji, Magnetorotational instability of dissipative Couette flow, J. Fluid Mech. **462**, 365 (2002).

[14] G. Rüdiger, M. Schultz, and D. Shalybkov, Linear magnetohydrodynamic Taylor-Couette instability for liquid sodium, Phys. Rev. E **67**, 046312 (2003).

[15] W. Liu, J. Goodman, and H. Ji, Simulations of magnetorotational instability in a magnetized Couette flow, Astrophys. J. **643**, 306 (2006).

[16] W. Liu, Numerical Study of the magnetorotational instability in Princeton MRI experiment, Astrophys. J. **684**, 515 (2008).

[17] C. Gissinger, J. Goodman, and H. Ji, The role of boundaries in the magnetorotational instability, Phys. Fluids **24**, 074109 (2012).

[18] P. A. Gilman and E. R. Benton, Influence of an axial magnetic field on the steady linear Ekman boundary layer, Phys. Fluids **11**, 2397 (1968).

[19] G. Siran, The effect of the electric conductivity of the Earth's mantle on the Ekman–Hartman hydromagnetic boundary layer and on the magnetic diffusion region, Stud. Geophys. Geod. **18**, 248 (1974).

[20] J. Szklarski and G. Rüdiger, Ekman-Hartmann layer in a magnetohydrodynamic Taylor-Couette flow, Phys. Rev. E **76**, 066308 (2007).

[21] J. L. Guermond, R. Laguerre, J. Léorat, and C. Nore, Nonlinear magnetohydrodynamics in axisymmetric heterogeneous domains using a Fourier/finite element technique and an interior penalty method, J. Comput. Phys. **228**, 2739 (2009).

[22] X. Wei and R. Hollerbach, Instabilities of Shercliffe and Stewartson layers in spherical Couette flow, Phys. Rev. E **78**, 026309 (2008).

[23] R. Hollerbach, Non-axisymmetric instabilities in magnetic spherical Couette flow, Proc. R. Soc. London, Ser. A **465**, 2003 (2009).

[24] R. Salmeron, A. Königl, and M. Wardle, Radial and vertical angular momentum transport in protostellar discs, Astrophys. Space Sci. **311**, 81 (2007).